Nanoscale

PAPER

View Article Online
View Journal | View Issue

Cite this: *Nanoscale*, 2025, **17**, 18678

Controlling the structural and sodium storage properties of glucose-derived hard carbons using the pre-carbonization heating rate†

Sofiia Prykhodska,[a] Konstantin Schutjajew,[a,b] Laura Kalder,[c]
Marius Hermesdorf,[a] Erik Troschke,[a] Desirée Leistenschneider,[a,d]
Falko Langenhorst,[d,e] Eneli Härk*[f] and Martin Oschatz*[a,b,d]

Received 12th March 2025,
Accepted 2nd July 2025

DOI: 10.1039/d5nr01053e

rsc.li/nanoscale

Non-graphitizing (so-called "hard") carbons, derived from natural and abundant precursors such as biomass, sugars (*e.g.*, glucose and sucrose) and polysaccharides (*e.g.*, starch and cellulose), are widely investigated as negative electrode materials for alkali metal-ion storage in secondary batteries because of their suitable structural features, including the unique "closed porosity". The formation of such microstructures depends on the heating conditions, such as the temperature or holding time of either carbohydrate condensation during preliminary carbonization ("pre-carbonization") or final carbonization. Numerous studies have extensively examined the impact of condensation and carbonization temperatures on the microstructure of hard carbons and their resulting electrochemical properties. Comparatively less research attention has been devoted to the influence of the heating rate in the low-temperature region, where it can be expected that the structure of the final hard carbon is largely established and a significant impact can be expected. Hence, this work is dedicated to investigating the effect of the rate of preheating, from room temperature to 600 °C, of glucose-derived carbon on its structure and electrochemical properties after final high-temperature carbonization at 1500 °C. Hard carbons obtained using 2, 10 and 200 K min^{-1} pre-carbonization temperature ramps exhibit distinct differences in plateau capacity values for sodium (226 ± 15.60 mAh g^{-1}, 206 ± 13.27 mAh g^{-1}, and 192 ± 9.44 mAh g^{-1}, respectively). This points to differences in closed porosity, defectiveness, and pore symmetry. The material preheated at the slowest ramp has the highest internal surface area, defectiveness, and highly asymmetrical pores, thereby promoting an increase in specific sodiation capacity (326 ± 21 mAh g^{-1}), particularly pronounced in the plateau region (226 ± 15.60 mAh g^{-1}). These findings imply the potential to regulate the microstructure of hard carbons through the initial heating rate during carbonization.

Introduction

Since the commercialization of the graphite-$\mathrm{LiCoO_2}$ system in 1991, lithium-ion batteries (LIBs) have played a crucial role in the development of portable electronics and electric vehicles.[1] Their rapid advancement sped up the evolution of large-scale energy storage systems.[2] The demand for lithium-ion batteries is set to triple by 2030, reaching over 3 TWh, highlighting a significant expansion in the market.[3] However, concerns, such as the imbalanced distribution of lithium across the world, human rights issues regarding water delivery to the local population in the "Lithium Triangle", resilience of supply, and political issues cause intensification of the development of alternative battery technologies from the laboratory to an industrially relevant scale.[4]

Sodium-ion batteries (SIBs) are considered as an emerging complement to LIBs, particularly in large-scale energy storage applications. This technology promises reduced cost, caused by the use of abundant resources, competitive cycling performance, and capacity retention due to comparable properties of Na to Li.[5,6] Nevertheless, the different charge densities of both ions significantly affect the cell chemistry at the negative electrode; that is, no suitable binary intercalation compounds with graphite can be formed by Na.[7,8] In view of this, research on

---

[a] *Friedrich-Schiller-University Jena, Institute for Technical Chemistry and Environmental Chemistry, Philosophenweg 7a, 07743 Jena, Germany. E-mail: martin.oschatz@uni-jena.de*

[b] *Helmholtz Institute for Polymers in Energy Applications Jena (HIPOLE Jena), Lessingstrasse 12-14, 07743 Jena, Germany*

[c] *Institute of Chemistry, University of Tartu, Ravila 14a, 50411 Tartu, Estonia*

[d] *Center for Energy and Environmental Chemistry Jena (CEEC Jena), Philosophenweg 7a, 07743 Jena, Germany*

[e] *Institute of Geosciences, University of Jena, Carl-Zeiss-Promenade 10, 07745 Jena, Germany*

[f] *Institute of Electrochemical Energy Storage, Helmholtz-Zentrum Berlin für Materialien und Energie GmbH, Hahn-Meitner-Platz 1, 14109 Berlin, Germany. E-mail: eneli.monerjan@helmholtz-berlin.de*

† Electronic supplementary information (ESI) available. See DOI: **https://doi.org/10.1039/d5nr01053e**

suitable negative electrode materials for SIBs is of ever-increasing importance. So far, non-graphitizing hard carbons (HCs) have been considered promising alternatives to graphite among the sp^2 carbon family for SIBs. This is due to their suitable working potential, favourable capacities, relatively low cost as compared to alloying and conversion-type materials, and long cycle life.[9–13] HC synthesis by the pyrolysis of renewable and low-cost carbon-rich organic precursors, such as various carbohydrates and biomass, meets the requirements of environmental compatibility and large-scale accessibility.[14–16] HCs exhibit structures of enormous complexity. Their understanding and further modification are critical to achieve controlled and targeted improvement of the electrochemical performance. Therefore, over the past few years, extensive research has focused on the correlation between the structural and electrochemical characteristics of HCs.[17,18] One of the generally accepted approximations is that the structure of HCs can be explained as an assemblage of two different carbon motifs. They consist of randomly oriented, defective, turbostratically stacked "graphite-like" nanosheets with enlarged interlayer distances (>0.335 nm) and graphene-like cross-links curved away from a planar geometry.[19] This arrangement results in unique nanoporosity, which is, however, often not accessible to the adsorptive molecules or atoms in standard physisorption measurements, or to some of the liquid electrolyte compounds (*e.g.*, the solvent) during battery operation. Although the exact mechanisms of sodium storage in HCs are still being debated, according to one of the most reasonable sodium storage mechanisms proposed by Stevens and Dahn,[20,21] in the "sloping region" of the charge–discharge profile, where the potential *vs.* Na/Na^+ continuously decreases, sodium intercalates into the domains of extended graphitic layers. In the so-called "plateau region", characterised by nearly constant potential, and, thus, a significant portion of electron transfer between the electrode and the metal, sodium forms metallic clusters inside the internal pores. Such metallic phases were detected and discussed as the main contributor to storage capacity in several small-angle X-ray scattering (SAXS) studies, as well as solid-state NMR investigations.[22–26] Considering all these facts, in recent years, more and more attention has been given to gaining control over alterations in the HC microstructure.[27–32] An illustrative example of the description of this microstructure is the "falling cards model" proposed by Dahn *et al.* The model explains the formation of closed pores by reorientation of graphene sheets during temperature treatment.[33] Several studies confirm the effect of pyrolysis conditions such as final carbonization temperature, heating rate or holding time on this microstructure and, thus, on the internal specific surface area (SSA) and ultimately the electrochemical performance of HCs.[34–40] However, before a complex carbon structure is ultimately set at the final temperature, numerous chemical reactions take place in the precursor systems already during condensation and pre-carbonization at lower temperatures. In the first approximation, these include C–H, C–OH, and C–C bond cleavage with subsequent formation of free radicals, rearrangement of molecules, condensation, elimination of side chains, and phase transitions.[41] These reactions take place at temperatures far below 1000 °C and are decisive for the structure of HCs, even if finally a treatment at higher temperatures is applied to achieve full carbonization. To set the relevant structural motifs of HCs such as closed pores and layer distances, the temperature range of 350–600 °C is anticipated to be crucial, since it has been reported as the main decomposition region of glucose-derived hydrothermal carbons.[42] It can, thus, be expected that the heating rates in this temperature region should have a major impact on the structural evolution of the final HC microstructure. Generally, it has been reported that a low heating rate (0.25–2 min^{-1}) during pyrolysis is advantageous to fabricate HCs for high reversible capacity and cycling stability.[43,44] For the rapid preparation (300 °C min^{-1}), a spark plasma sintering technology, which integrates field-assisted sintering, plasma activation, hot pressing, and resistance heating, has been developed.[45] Meanwhile, it has been identified that preliminary carbonization at temperatures below 600 °C plays a significant role in enhancing the electrochemical performance of HCs.[46,47] Additionally, Kamiyama *et al.* observed an enhancement in plateau capacity for MgO-templated hard carbon pre-carbonized at 600 °C.[29] However, the influence of the heating rate of the preliminary carbonization has not yet been investigated in depth. Therefore, in this study, it was examined how pre-carbonization at various heating rates, up to 600 °C, of glucose hydrothermal spheres impacts the final carbon structure after treatment at 1500 °C. The final carbonization temperature was selected based on the study of Au *et al.*,[35] which reported this temperature as the most favorable for achieving improved electrochemical performance of hydrothermal carbons. By combining data from wide-angle X-ray scattering (WAXS), SAXS, and gas physisorption techniques, to analyze the electrochemical data in HC-sodium half-cells, an empirical link between structural factors and sodium storage

Martin Oschatz

Martin Oschatz studied chemistry at the Technische Universität Dresden. He carried out his Ph.D. studies in the group of Stefan Kaskel and graduated in 2015. In 2013, he undertook a research stay with Gleb Yushin at Georgia Tech. After a postdoctoral stay at Utrecht University in the group of Krijn de Jong, Martin joined the Colloid Chemistry Department led by Markus Antonietti at the MPI of Colloids and Interfaces in November 2016. Since 2021, he has been a full professor at Friedrich Schiller University Jena. His research is focused on nanostructured carbon-based materials for energy and environmental applications.

is established. For a series of three samples prepared with different pre-carbonization rates, namely 2, 10 and 200 K min^{-1}, it was found that, despite a comparable degree of carbonization, parameters, such as internal surface area, pore asymmetry, and defectiveness, increased for the HC that was preheated at the slowest rate. These structural properties of HCs are beneficial for reversible sodium storage capacity, particularly in the plateau region (below 0.1 V). Conversely, the fastest preheated HC displays a decrease in sodiation capacity. The observed trends could be attributed to differences in glucose condensation and decomposition and/or to the trapping of precursors within the structure during slow preheating, wherein they can subsequently act as templates at elevated temperature. While the structural variances may appear minor upon initial observation, this study sheds light on the control of material structures during intermediate low-temperature processing. It, thus, offers insights into the future design, development, and characterization of non-graphitizing carbons with adjustable porosity as negative electrode materials for SIBs.

Experimental

Synthesis of materials

Hard carbons were prepared by hydrothermal carbonisation of glucose, followed by two-stage high-temperature treatment, divided into pre-carbonization and final carbonization. Typically, 10 g D-glucose (≥99%, Sigma Aldrich) was dissolved in 62.5 mL of distilled water. The solution was transferred into a 100 mL Teflon-lined stainless-steel autoclave, subsequently heated to 200 °C and kept for 12 h (drying oven DRY-Line Prime, VWR). The resulting gel-like material was dried at 160 °C for 6 h (drying oven DRY-Line Prime, VWR). After grinding in a mortar, the powder was placed in a porcelain-combustion boat and pre-carbonized at 600 °C for 1 h under a N_2 flow with heating rates of 2, 10 and 200 K min^{-1}. Preliminary carbonizations at rates of 2 K min^{-1} and 10 K min^{-1} were carried out in a horizontal tube furnace Carbolite Gero. An infrared furnace, Behr IRF, 10 was used for applying a 200 K min^{-1} heating rate. A holding time of 1 hour was applied for all samples. The final carbonization was conducted in a high-temperature oven LORA, HTM Reetz at 1500 °C for 2 h under a N_2 flow with an identical heating rate of 3 K min^{-1}. The resulting materials after pre-carbonization were labeled as HC-*X*-600, and those after the final heat treatment were denoted as HC-*X*–600–1500, where *X* refers to the heating rate applied during the pre-carbonization stage. For recording Fourier-transform infrared (FTIR) spectra of intermediates, hydrochar of glucose obtained hydrothermally at 200 °C was heated to different temperatures under a N_2 flow at heating rates of 2 and 10 (Carbolite Gero horizontal tube furnace) and 200 K min^{-1} (Behr IRF 10 infrared furnace), respectively, with a holding time of 1 minute. The resulting samples were named HC-*X*–*Y*, where *X* refers to the heating rate and *Y* to the temperature at which the intermediate was obtained.

Characterization of the materials

N_2 and CO_2 physisorption measurements were carried out on a volumetric gas sorption analyser (Quantachrome Quadrasorb) at −196 °C and 0 °C, respectively. Quenched-solid density functional theory (QSDFT, for N_2 at 77 K on carbon surfaces with slit/cylindrical pores and adsorption branch kernel) and a non-local density functional theory model (NLDFT, for CO_2 at 273 K on carbon) were used to determine the pore/ultramicropore volume, pore size distributions, and specific surface areas available for the adsorptive molecules. Ar isotherms of intermediates were recorded at −186 °C using a Vapor200C gas sorption analyzer from 3P Instruments. Quenched solid density functional theory (QSDFT) from the adsorption branch of the Ar isotherm for cylindrical/sphere shaped carbon pores was used to calculate the pore size distributions and specific surface areas. H_2O vapor adsorption/desorption isotherms were recorded volumetrically using an Autosorb IQ apparatus (Quantachrome Instruments). The analysis temperature was controlled using a circulating-bath temperature controller with an accuracy of 0.1 K. Before N_2, CO_2, and Ar gas physisorption measurements, samples were outgassed at 150 °C under vacuum for 24 h. For H_2O vapor sorption experiments, samples were outgassed at 200 °C under vacuum for 24 hours.

X-ray photoelectron spectroscopy (XPS) was conducted with a K-alpha spectrometer from Thermo Fisher Scientific. All samples were fixed on adhesive Cu-tape. For charge compensation, a flood gun was used during the measurement, which was calibrated to C═C in PE 284.8 eV ± 0.1 eV. Therefore, the binding energy was not further corrected. The measured spot size was 400 μm for each sample. For compositional data, a survey spectrum with a step size of 1 eV and a pass energy of 100 eV was recorded. High-resolution spectra were recorded with a step size of 0.05 eV and a pass energy of 30 eV and 3–5 scans for each element. The data were analysed using Avantage v6.6.0 from Thermo Fisher Scientific.

For transmission electron microscopy (TEM) investigations, materials were loaded onto holey carbon grids and images were acquired using a 200 kV FEI Tecnai G2FEG equipped with an Oxford 80 mm^2 energy-dispersive silicon drift X-ray detector and a Gatan UltraScan 2k CCD camera. Raman spectra of HCs were obtained on a Raman microscope (inVia, Renishaw, 633 nm laser wavelength, 50× LWD objective). Spectra were recorded in the range of 500–3600 cm^{-1} with three accumulations at a laser power of 3.5 mW. The spectra were separately fitted using Lorentzian functions in OriginPro 2021 software assuming a 4-band model.[48] The I_D/I_G and I_A/I_G ratios were determined from the peak maximum intensities obtained through the fitting procedure.

Carbon, hydrogen, nitrogen, and sulfur (C/H/N/S) elemental analysis (EA) was performed using a Vario Micro device *via* combustion analysis. The oxygen content was determined by subtracting the measured amounts of carbon, hydrogen, and nitrogen from 100% (sulfur content was below the detection limit in all cases). Wide-angle X-ray scattering (WAXS) patterns were recorded on a Bruker D2 Phaser and a Bruker D8 Advance with Bragg–Brentano geometry in a 2θ range of 10–70° with a step size of 0.02° using CuKα (λ = 0.154 nm) radiation. The anode voltage was 30 kV and the anode current was 10 mA. A horizontal silicon single crystal was used as a sample holder. The structural parameters were determined by applying the Ruland and Smarsly algorithm to the measured data.[49–52]

Small-angle X-ray scattering (SAXS) measurements were conducted using the custom-built FlexSAXS system at Helmholtz-Zentrum Berlin. SAXS data were collected with a DECTRIS PILATUS3 100K-M detector at a fixed distance of 20.12 cm. All samples were measured in a vacuum with a custom-made sample holder, using an IμS HIGHBRILLIANCE CuKα Microfocus X-Ray source and an exposure time of 5.3 seconds. Background scattering intensities were measured separately under identical conditions. A sample thickness of 0.2 mm was used for data reduction, and the data were corrected for the respective sample transmission values. Scattering of the samples was acquired within the scattering vector range of $0.1 < q < 7$ nm^{-1}. The apparent density of the carbon powder was used to normalize the macroscopic scattering cross-sections, yielding units in the cm^2 g^{-1} range. Normalized scattering intensities *vs.* scattering vector curves can be used to directly analyse several structural parameters in a model-free manner. This analytical method has been successfully utilized in several prior studies.[30,53–55] Therefore, a detailed explanation of the analytical process is provided in the ESI.† FTIR spectra were acquired using a Shimadzu IR Spirit QATR-S FTIR spectrometer. Thermogravimetric analyses (TGA) were performed on a Netzsch STA 449 in Al_2O_3 crucibles under N_2 in a temperature range from 25 °C to 1000 °C at a fixed heating rate of 2 as well as 10 K min^{-1}.

Electrochemical measurements

Typically, 135 mg of active material was mixed with 7.5 mg of conductive carbon black Super C65 (Imerys Graphite & Carbon) as well as 375 µl of 20 mg ml^{-1} water solution of carboxymethylcellulose (CMC) from Sigma Aldrich. The mixture was treated in an impact ball mill, Fritsch PULVERISETTE 23, at 50 Hz for 3 minutes. The obtained slurry was coated onto carbon-covered aluminium foil (MTI Corporation) using a doctor blade at 100 µm wet film thickness at 30 mm s^{-1}. All electrodes were dried for 24 hours in a vacuum oven at 70 °C, and then discs of 12 mm diameter were punched from the electrode sheets for half-cell measurements. The areal loading of the electrodes ranged from 2.03 to 2.32 mg cm^{-2}, primarily depending on the filling density of the active material. Electrochemical experiments were performed in a two-electrode setup using Swagelok-type cells and a Biologic MPG-2 potentiostat. Sodium metal (Sigma Aldrich) discs were applied as counter and reference electrodes. The electrolyte was 1 M $NaPF_6$ in a 6 : 4 v/v mixture of ethylene carbonate (EC) and diethyl carbonate (DEC). The amount of electrolyte in each half-cell was 150 µL. A Celgard 2310 PEO membrane (Asahi Kasei Corporation) along with a glass fibre filter (Whatman GF/C, GE Healthcare) was used as a separator. The applied current densities were chosen with respect to the theoretical capacity of a Li-graphite anode (C_{372} = 372 mAh g^{-1}). The bulk sodium plating capacity was determined at $C/20$ (18.6 mA g^{-1}), as the capacity at which the crystallization overpotential occurred, by intentionally oversodiating the HC electrode after cycling in a voltage range of 2.5–0.002 V for six cycles.[56]

Results and discussion

Structural characterization

The TGA data of the hydrochar, recorded at different heating rates, provide initial insight into the kinetics of the pre-carbonization. As can be observed, until approximately 340 °C, the heating rate does not significantly impact the mass reduction (Fig. S1a†). However, above this temperature, fast heating results in a slightly lower mass loss, and at 600 °C, this difference becomes more pronounced. This, in turn, points to altered kinetics of the rearrangement of native carbon motifs in condensation reactions in the previously reported main decomposition region.[42]

FT-IR spectra offer information about changes in functionalities that occur during heat treatment. The spectra of samples heated up to 300 °C still display comparable stretching vibrations to those of the hydrochar (ν(OH) ≈ 3500 cm^{-1}; ν(C–H$_{\text{aliphatic}}$) ≈ 2970 cm^{-1} for methyl groups and ≈2925 cm^{-1} for methylene groups; ν(C═O) ≈ 1705 cm^{-1}; and ν(C═C) ≈ 1606 cm^{-1}).[42,57,58] The signal around 798 cm^{-1} corresponds to the aromatic C–H out-of-plane bending vibrations (δ(C–H$_{\text{out of plane}}$)) (Fig. S1b†).[59] Nevertheless, compared to hydrochar, HC-*X*–300 exhibits an enhancement of C═C and a reduction in C═O stretching bands, along with no significant changes in δ(C–H$_{\text{out of plane}}$), reflecting oxygen loss and ring condensation without significant structural reorganization. This behavior is typical for heat treatments at low temperatures.[60] Relatively modest changes, however, are observed for HC-200–300, suggesting that the material is more carbon-rich, likely as a result of faster reaction kinetics. After 450 °C, the most prominent decrease in the intensity of C═O and C═C stretching vibrations is observed for the carbon obtained at the highest heating rate (HC-200–450) (Fig. S1c†). Furthermore, the appearance of the C–H$_{\text{aromatic}}$[57] stretching vibration at approximately 3040 cm^{-1}, along with well-resolved spectral bands at 874, 811, and 749 cm^{-1} (δ(C–H$_{\text{out of plane}}$)),[61] reflects a structural evolution towards a more aromatic material compared to HC-2–450 and HC-10–450.

After 600 °C, when preliminary carbonization is completed, all samples exhibit FT-IR spectra with decreased oxygenated functionalities and increased aromatic domains, typical for carbons obtained at that temperature (Fig. S1d†).[42,62] Furthermore, spectra show that all materials are chemically comparable. This is further confirmed by elemental analysis (Table S1†) and XPS (Fig. S2 and Table S2†).

After high-temperature treatment, the transmission electron microscopy images recorded at lower magnifications show that HC-*X*–600–1500 carbons retain a spherical morphology, and the diameter of the spheres is in the range of 0.5–2 μm (Fig. S3a–c†). At higher magnifications, TEM images of HC-*X*–600–1500 (Fig. S3d–f†) demonstrate turbostratic microstructures composed of mostly disordered domains, which is typical for hard carbons prepared at 1500 °C.[35]

Raman spectroscopy provides insights into the chemical binding motifs within the carbon materials, as well as their carbonization/graphitization degree. Typically, hard carbons exhibit broad peaks around 1355 (D-band) and 1581 cm^{-1} (G-band), related to in-plane sp^2 C-bond breathing (at graphite defects) and stretching modes. Thus, the intensity ratio between G and D peaks (I_D/I_G) provides information about the degree of defectiveness and disorder, if a perfectly ordered graphitic material is taken as the reference.[63,64] An additional sign of disorder arises from the A-band (1483 cm^{-1}), situated between the D- and G-bands, stemming from amorphous structures. Generally, all HC-*X*–600–1500 materials exhibit a well-organized structure resulting in distinct Raman peaks, as anticipated following thermal treatment at 1500 °C (Fig. S4†). The A-band displays low intensity across all samples, while the overtones of D + G and 2D (2898 and 2652 cm^{-1}, respectively) are observable. The comparable values of I_D/I_G and I_A/I_G ratios suggest similarities in the microstructure across the samples (Table S3†). The same phenomenon is also observed in the carbons obtained after 600 °C (Fig. S5†).

Using wide-angle X-ray scattering analysis, the microstructure of the non-crystalline carbon materials was further investigated. The algorithm of Ruland and Smarsly for fitting the WAXS patterns was applied in order to allow for the quantification of parameters, such as the expansion of graphitic regions in lateral and stacking directions, which then can be correlated well with electrochemical data.[65] Ordinarily, the WAXS patterns of HC-*X*–600–1500 (Fig. S6†) demonstrate the characteristic reflections of disordered hard carbon materials, corresponding to (002), (100), and (110) planes.[66] It is important to note that the Ruland and Smarsly algorithm focuses on the characteristic diffraction peaks of non-graphitic carbon, primarily the (002) and (100) reflections, and to a lesser extent, the (110) reflection. Signals originating from non-carbon components or the amorphous background are not considered. Despite this, the model exhibits deviations within ±1% for most of the profiles and remains within ±5% even in regions near the unresolved hump in the range of 0.6–0.7 Å^{-1}.[52] As can be observed, the 2 theta positions, as well as the intensities of reflections, are comparable for all materials. While the standard deviation of the first-neighbour distribution (indicating lateral disorder), σ_1, remains unchanged for all samples, parameters, such as the interlayer distance, a_3, the average stacking size, L_c, and the average number of graphene layers per stack, N, slightly increase with reducing pre-carbonization heating rate (Table 1). The average length of the graphene layer, L_a, is of the same order of magnitude for all hard carbons (Table 1). To summarize trends between all WAXS parameters, the microstructural differences between glucose-derived hard carbons are insignificant. This indicates that the microstructure of the investigated HCs is comparable. No remarkable differences in the microstructure are also revealed after treatment at 600 °C (Fig. S7 and Table S4†). This is consistent with the findings from Raman spectroscopy (Fig. S4, Table S3 and Fig. S5†).

The contrast in small-angle X-ray scattering is the difference in electron densities between vacuum (pores) and carbon throughout the sample; thus, SAXS allows for the detection of the entire porosity (*i.e.*, mesostructure). The SAXS patterns acquired for HC-*X*–600–1500 resemble those demonstrated in

Table 1 WAXS[a]/SAXS[b] parameters of HC-*X*–600–1500

Parameter	HC-2–600–1500	HC-10–600–1500	HC-200–600–1500	
L_a, nm	6.3 ± 1.3	7.1 ± 1.4	6.3 ± 1.3	
σ_1, nm	0.012 ± 0.001	0.013 ± 0.001	0.012 ± 0.001	
L_c, nm	0.77 ± 0.2	0.73 ± 0.2	0.66 ± 0.2	↓
N	2.12 ± 0.05	2.01 ± 0.06	1.81 ± 0.05	↓
a_3, nm	0.365 ± 0.002	0.363 ± 0.002	0.363 ± 0.002	↓
B_{fl}, $\text{cm}^2\ \text{g}^{-1}\ \text{nm}^{-2}$	18.4 ± 1.7	1.76 ± 0.5	0.84 ± 0.24	↓
P_m, $\text{cm}\ ^2\text{g}^{-1}\ \text{nm}^{-4}$	0.07 ± 0.01	0.02 ± 0.005	0.013 ± 0.002	
l_R, nm	0.9 ± 0.2	1.4 ± 0.3	1.4 ± 0.3	↑
S/m, $\text{m}^2\ \text{g}^{-1}$	769 ± 209	204 ± 57	175 ± 36	↓
Q_m, $\text{cm}^2\ \text{g}^{-1}\ \text{nm}^{-3}$	3.77 ± 0.48	1.34 ± 0.25	0.97 ± 0.17	↓
Φ	0.29 ± 0.04	0.10 ± 0.02	0.085 ± 0.015	↓
l_c/l_p	49.8 ± 15.38	22.6 ± 8.4	21.75 ± 6.4	↓
l_c, nm	42.5 ± 5.6	25.1 ± 4.7	26.9 ± 4.7	↓
l_p, nm	0.85 ± 0.24	1.11 ± 0.36	1.23 ± 0.29	↑
l_{solid}, nm	2.9 ± 0.90	10.82 ± 4.2	14.4 ± 4.32	↑
l_{pore}, nm	1.21 ± 0.52	1.24 ± 0.63	1.35 ± 0.54	
$\langle \Delta^2 a_3/{a_3}^2 + \Delta^2 l_R/{l_R}^2 \rangle$	0.62 ± 0.13	0.06 ± 0.023	0.033 ± 0.01	↓

L_a – average graphene layer extent – intralayer scattering; σ_1 – standard deviation of the first-neighbour distribution (shows lateral disorder); L_c – average stacking size; N – average number of graphene layers per stack; a_3 – average interlayer spacing – interlayer scattering component; B_{fl} – fluctuation component; P_m – Porod constant; S/m – inner surface; Q_m – invariant expressed per unit mass; l_R – lateral correlation length; ϕ – porosity; l_c – length of coherence; l_p – average chord length; l_c/l_p – anisometric ratio, describing the shape of the pores; l_{solid} – average chord length of pore walls; l_{pore} – average chord length of the pore; $\langle \Delta^2 a_3/{a_3}^2 + \Delta^2 l_R/{l_R}^2 \rangle$ – degree of disorder, interlayer spacing a_3 estimated from WAXS. [a] CarbX: a program for the evaluation of wide-angle X-ray scattering data of non-graphitic carbons.[75] [b] Model-free SAXS analysis.

the literature, suggesting the existence of a microporous structure, possibly even beyond the porosity detectable by gas sorption (Fig. S8†).[55,67] Parameters derived from SAXS are presented in Table 1. A simplified structural model is developed from this and will be correlated with the electrochemical data later as illustrated in Fig. 4. Generally, all carbons after high-temperature processing represent high total porosity. However, employing pre-carbonization with varying kinetics contributes to certain changes. The parameters ϕ and S/m, which are correlated with porosity and inner surface, respectively, reach their maximum values with the lowest pre-carbonization heating rate and conversely decrease with the higher one. It is also noticeable that the asymmetry of the pores, embodied in the ratio l_c/l_p, is the greatest for HC-2–600–1500; however, the pore size, l_{pore}, for all carbons is comparable. Interestingly, HC-200–600–1500 exhibits the thickest pore wall, l_{solid}, and this parameter decreases as the preheating rate decreases. Remarkably, HC-200–600–1500 has the thickest pore wall, l_{solid}, and this parameter decreases with a decrease in the preheating rate. The fluctuation component, B_{fl}, which describes defects on the surface, as well as the length of coherence, l_c, increases with decreasing pre-carbonization heating rate. This indicates that HC-2–600–1500 exhibits the surface with the highest level of defects. Furthermore, this is in line with the decrease in the parameter l_R, corresponding to the curvature of the graphene layer, and a slight increase in disorder $\langle \Delta^2 a_3/a_3^2 + \Delta^2 l_R/l_R^2 \rangle$. Therefore, it can be assumed that a fast preheating rate leads to the smoothing of structural defects, while a slow rate leads to higher defectivity. Moreover, a fast heating rate results in thicker pore walls and more curved carbon layers.

The scattering patterns of HC-*X*–600 samples, shown in Fig. S9,† draw the reader's attention to changes compared to those measured for HC-*X*–600–1500 (Fig. S8†), particularly within the micropore length scale range, relevant to the sodium nucleation and sodiation mechanism discussed in the Electrochemical characterization section. The scattering data immediately reveal intensity shifts and curve broadening, primarily characteristic of microporous carbon around $q > 1\ \text{nm}^{-1}$, indicating localized changes in pore architecture. The model-free analysis failed to reliably quantify the proportion of lateral imperfections in the carbon layers caused probably by the precursor being trapped in the structure; therefore, this approach was not applied to HC-*X*–600 samples.

Generally, a high volume of open porosity correlates with a significant decrease in the energy density of the cell, due to the formation of an inactive mass of the solid-electrolyte interface (SEI) during the first cycle.[12,68,69] Thus, N_2, CO_2 and H_2O vapour sorption experiments are conducted to provide details on the open porosity of HC-*X*–600–1500. N_2 physisorption isotherms of HC-*X*–600–1500 (Fig. 1a) can be classified as IUPAC Type-II, which is typical for non-porous materials.[70] The surface areas determined by the QSDFT method are between 11 and 15 m^2 g^{-1}, demonstrating comparable and low nitrogen accessible porosity for all carbons. It is noteworthy that ultramicropores (<0.7 nm), as well as closed pores, are undetectable by N_2 physisorption, mostly due to restricted diffusion under cryogenic conditions.[70] Because of the elevated diffusion at higher temperatures and smaller kinetic diameter, CO_2 physisorption at 273 K emerges as a preferable technique for exploring such ultramicropores.[71] Upon analyzing the CO_2 physisorption isotherms of HC-*X*–600–1500 (Fig. 1b), a discernible difference in porosity between the carbons is detected. The isotherm of HC-2–600–1500 displays the highest gas uptake at 1 atm pressure among all HC-*X*–600–1500, whereas HC 200–600–1500 shows the lowest. The pore size distribution and cumulative pore volume, calculated using the NLDFT model (Fig. S10†), indicate that a reduction in the heating rate during pre-carbonization results in an increase in ultramicropore volume (particularly for pores smaller than 0.3 nm) after high-temperature treatment, while remaining within the typical range for hard carbons prepared at 1500 °C.[35,72] Due to the smaller kinetic diameter of the adsorptive (0.265 nm) and the higher measurement temperature (298 K), H_2O vapor physisorption is capable of resolving information on pores smaller than 0.5 nm, inaccessible even to CO_2 at 273 K.[71,72] Typically, the H_2O isotherms of HC-*X*–600–1500 (Fig. 1c) exhibit an S-shaped curve and hysteresis loop and are classified as Type V according to the IUPAC regulations, pointing to microporous carbon.[70] The adsorption branches for all carbons exhibit a

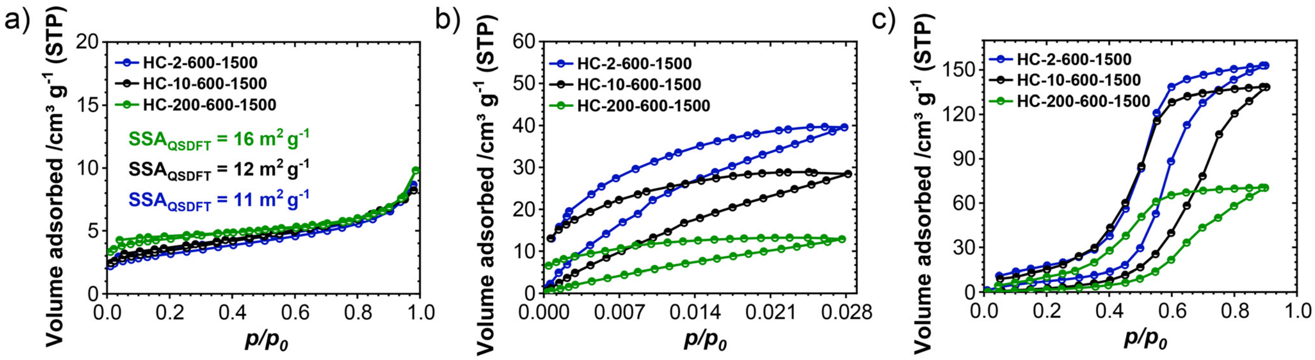

Fig. 1 Sorption isotherms of the investigated glucose-derived hard carbons after final carbonization: (a) N_2 physisorption isotherms at 77 K; (b) CO_2 physisorption isotherms at 273 K; (c) H_2O vapour physisorption isotherms at 298 K.

very low vapor uptake at low relative pressure, which is characteristic of a hydrophobic surface.[73] The strength of the interaction between H_2O and the carbon surface and thus the hydrophilicity/hydrophobicity, is strongly dependent on the oxygen content.[74] Therefore, the observed hydrophobicity is consistent with the low oxygen content (<2%) revealed by elemental analysis (Table S5†). H_2O vapor uptakes are significantly greater than N_2 uptakes despite similar relative pressure ranges of the measurements and follow a trend similar to that of the CO_2 uptakes (Fig. 1b). Furthermore, the adsorption isotherms nearly reach saturation and the desorption isotherms show nearly fully reversible behaviour with complete vapor removal. This shows that water vapor is a highly suitable adsorptive to detect porosity that appears closed for N_2 at 77 K, in general, and the differences arising in this closed porosity for different pre-carbonisation heating rates. It becomes evident that the slow heating rate during the pre-carbonization correlates with the enhancement of closed ultramicroporosity present in the HC after high-temperature carbonization. These findings corroborate the data provided by SAXS (Table 1).

Alterations in the mesostructure become discernible after 600 °C, when pre-carbonization is complete. Changes can be detectable with adsorbates with a larger kinetic diameter, such as Ar. As shown by the Ar physisorption data at 87 K (Fig. S11a†), a slow rate during restructuring and condensation of carbon motifs contributes to an increase in porosity and promotes the formation of micropores smaller than 2 nm (Fig. S11b†). This observation, in combination with SAXS data (Fig. S9†), suggests that in HC-2–600, the precursor might be trapped in the structure and act as a template during subsequent heating, thereby contributing to the enhancement of porosity. Nevertheless, the distinctions in very small pores detected by CO_2 (<0.7 nm) and H_2O (<0.5 nm) are not substantially pronounced (Fig. S12†).

As a whole, it is demonstrated by the structural characterization of the investigated materials that the heating rate in the critical low-temperature region does not have a significant effect on the atomic construction of the carbon frameworks ("microstructure"). However, a considerable impact on the mesoscale structure such as porosity is observed both after preliminary carbonization and following subsequent high-temperature treatment. As will be shown in the following, these differences are responsible for changes in the electrochemical behaviour.

Electrochemical characterization

In order to investigate the structural influence on sodium storage performance, galvanostatic charge–discharge (GCD) experiments at a low current density of 18.6 mA g^{-1} were conducted in the voltage window of 2.5–0.002 V. Furthermore, capacity limited experiments were carried out due to the demonstration of additional reversible capacity until the onset of sodium nucleation determined by crystallization overpotential at values below 0 V *vs.* Na/Na^+.[56] In the first cycle (Fig. 2a), all hard carbons exhibit coulombic efficiency (CE) values not lower than 82 ± 5.11% (Fig. 2b). These values are comparable to those of HCs prepared at a slow overall pyrolysis heating rate.[43,44] The insignificantly lower CE of HC-2–600–1500 (Fig. 2b) may be attributed to additional small ultramicropores, leading to the introduction of more accessible sites for electrolyte decomposition.[12,68,69] This observation aligns with the porosities unveiled by CO_2 and H_2O sorption measurements (Fig. 1b and c).

Analysis of the 2nd sodiation cycle allows monitoring changes that may occur after initial cycling. The CE values in the 2nd cycle show a similar trend to those in the 1st cycle (insets, Fig. 2c and b). It may suggest continued stabilization of the SEI or further side reactions, according to the reference.[76] A notable variance in sodiation capacity is evident among the samples. As can be observed, the specific sodiation capacity increases with decreasing pre-carbonization heating rate (Fig. 2c). Upon examination of both the sodiation capacities in the slope (above 0.1 V) and plateau (below 0.1 V) regions, it is evident that, despite only a minor difference in slope capacities, considerable variation persists in the plateau stage (Fig. 2d). It has been demonstrated by L. Kalder *et al.*[65] that the average interlayer spacing a_3, obtained from WAXS, has a more significant impact on the sodiation slope region; meanwhile, the L_a/l_R ratio is decisive for both slope and plateau sodiation capacities. Hence, a combination of these parameters could be applied to estimate the electrochemical performance of hard carbons. In this study, these correlations were employed to gain insight into the impact of the pre-carbonization rate on sodium storage. Generally, within the slope region there are no pronounced differences in capacity. This observation is consistent with the observation in microstructural characteristics, in particular, with the interlayer distance a_3 (Table 1). The most graphitized HC-2–600–1500 stands out in slope capacity (Fig. 2e). The curvature of the graphene layer, represented by l_R, sheds light on the performance differences among hard carbons. Despite unremarkable alterations in the slope region, the plateau capacity decreases as l_R increases (Fig. 2f). It can lead to the assumption that, for HC-*X*–600–1500, excessive curvature of graphene sheets, stemming from rapid heating in the crucial low-temperature region, is not beneficial for sodium storage. Since L_a is found to be comparable for all HC-*X*–600–1500 (Table 1), it fails to elucidate the discrepancy observed in the sodiation sub-regions. The current study further corroborates that optimal sodium storage performance is achieved with a graphene layer length of approximately 6.3 ± 1.3 nm and a curvature of 0.9 ± 0.2 nm, consistent with the findings reported by L. Kalder.[65] However, it is important to emphasize that, although HC-10–600–1500 and HC-200–600–1500 exhibit comparable values for parameters L_a and l_R, the present results clearly demonstrate that a reduction in the thickness of the pore wall, l_{solid}, also plays a critical role in enhancing storage efficiency, *i.e.*, promotes the development of pores whose sizes are on the same order as the pore wall thickness. It is worth noting that several studies have reported that the presence of defective sites can enhance Na^+ adsorption and improve the sodiation process.[77,78] Therefore,

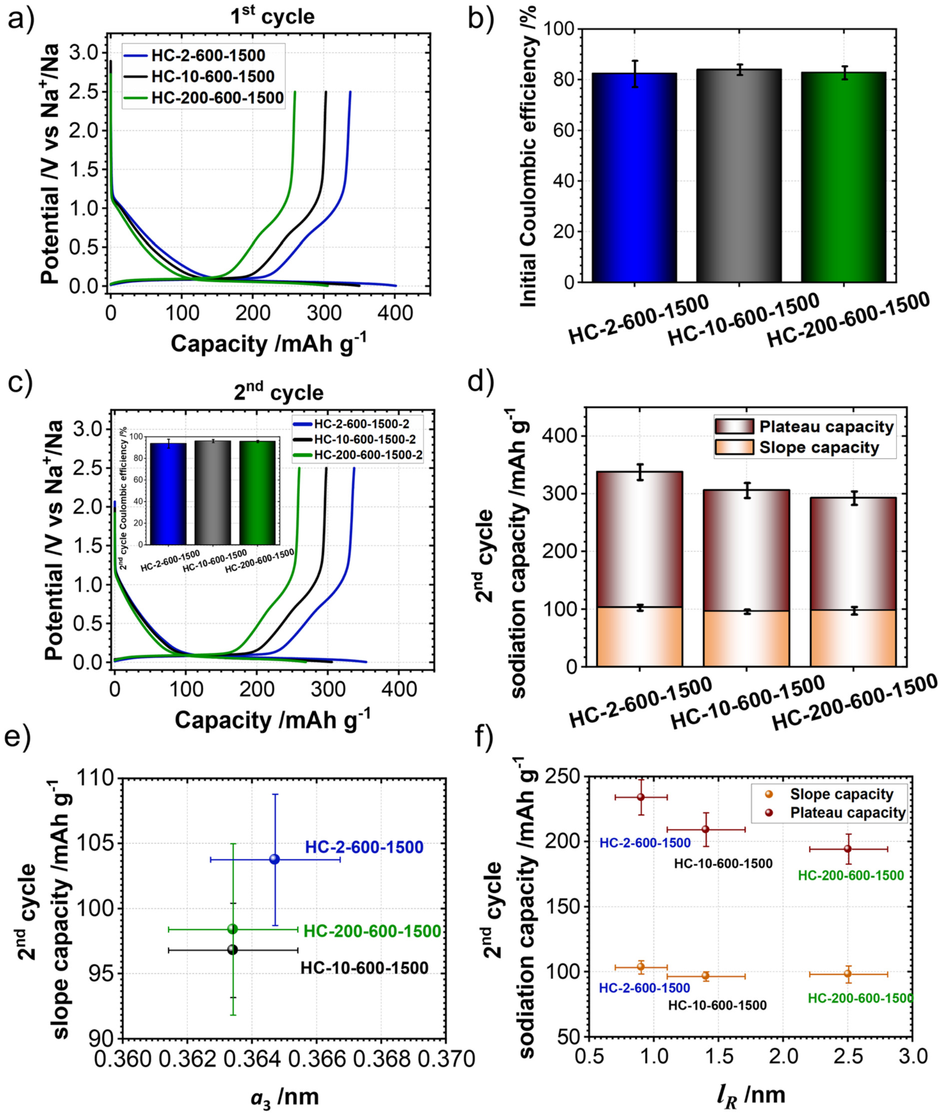

Fig. 2 Galvanostatic charge–discharge curves of glucose-derived hard carbons in Na-ion half cells recorded at a $C/20$ current density. (a) First cycle; (b) initial coulombic efficiency; (c) second cycle; (d) a bar graph representing slopes as well as plateau capacities in the second cycle. (e) Correlation between the average interlayer spacing a_3 and slope capacity in the second cycle; (f) correlation between the lateral correlation length, l_R, and slope and plateau capacities in the second cycle.

an increase in defectiveness, B_{fl}, (Table 1) appears to be advantageous for this process. Moreover, the highest inner surface area, S/m, observed for HC-2–600–1500 (Table 1) may contribute to enhancing the plateau capacity, provided that the plateau region corresponds to the clustering of sodium inside the internal pores.[12,79] Additionally, it has been reported that an increase in plateau capacity is associated with the less asymmetric shape of pores.[65] In this study, a hard carbon prepared at the lowest pre-carbonization heating rate exhibits the highest plateau capacity value, despite having the most asymmetric pores. The average pore size, l_{pore}, of this material is comparable to that of HC-10–600–1500 and HC-200–1500. Therefore, it is noteworthy that the interplay between a_3, l_R, B_{fl}, S/m, and l_c/l_p, observed in this study, contributes to the sodium ion storage, highlighting the primary alterations in the plateau region. Furthermore, the closed pore volume, $V_{\mathrm{closed\ pores}}$, estimated from the plateau capacity as described by Xiao *et al.*[79] (eqn (S16†)), exhibits an increasing trend with decreasing pre-carbonization heating rate (Table S6†).

A deeper understanding of the material's behaviour over the cycles is crucial for optimizing its performance in practical applications. Therefore, in order to assess whether changes in behaviour would occur during further cycling, the materials were additionally examined in the 5th cycle. By the 5th cycle, the SEI is typically stabilized and irreversible processes are minimized, resulting in improved CE with no significant differences among the samples. In this cycle, CE values for all materials are above 97 ± 1.00% (inset, Fig. 3a).[76] Similar to the 2nd cycle, carbon prepared at a slow pre-carbonization heating rate (HC-2–600–1500) represented the highest specific

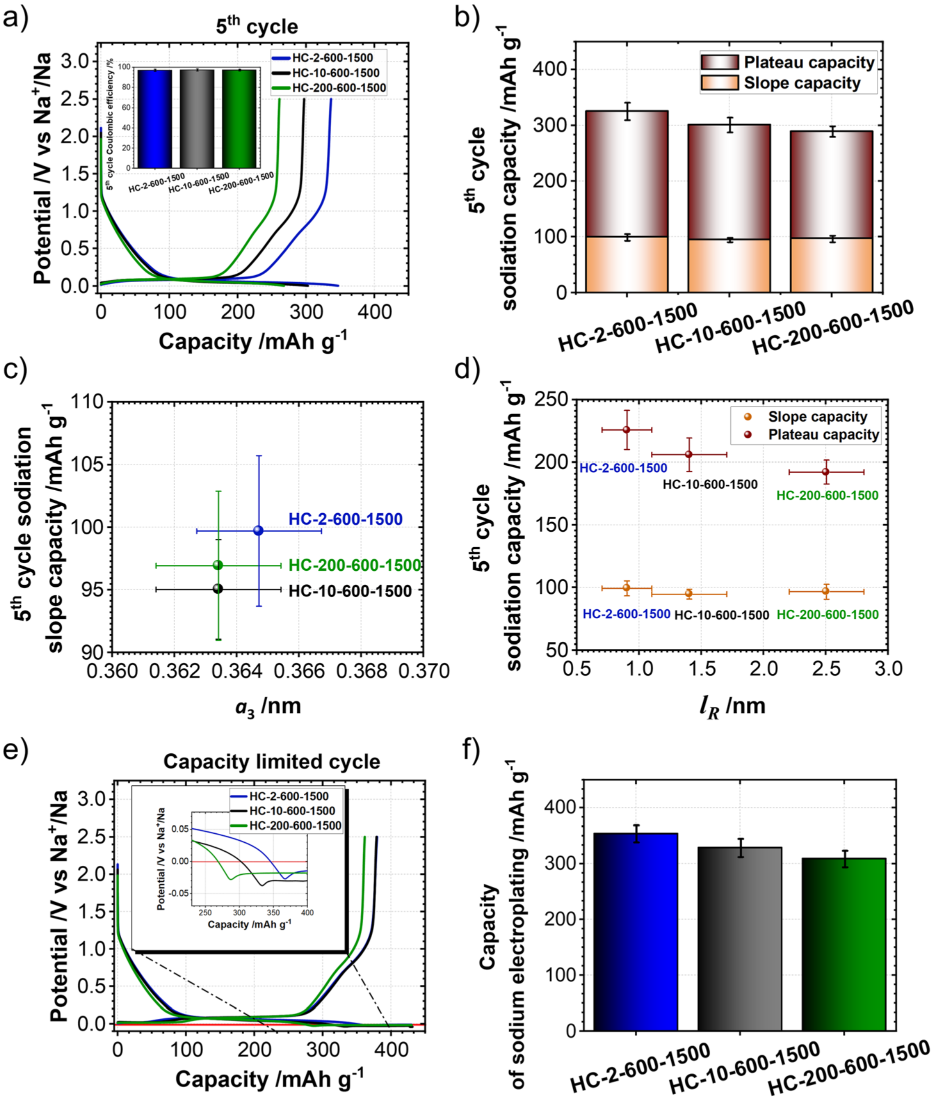

Fig. 3 Galvanostatic charge–discharge curves of glucose-derived hard carbons in Na-ion half cells recorded at a $C/20$ current density. (a) 5th cycle; (b) a bar graph representing slopes as well as plateau capacities in the 5th cycle; (c) correlation between the average interlayer spacing a_3 and the slope capacity in the 5th cycle; (d) correlation between the lateral correlation length, l_R, and slope and plateau capacities in the 5th cycle; (e) capacity limited cycle (8th); (f) capacity of sodium electroplating.

sodiation capacity values (Fig. 3a). Furthermore, the primary changes are observed in the plateau region (Fig. 3b–d).

In the capacity-limited cycle, the capacity values of the bulk sodium electroplating process change according to the trend in different pre-carbonizations (Fig. 3e and f). Namely, the highest capacity value corresponds to the slowest ramping until 600 °C. This confirms that this material can store the highest amount of sodium in the low plateau region, which is beneficial for achieving a higher energy density of the battery's negative electrode material.

To visualize the interplay of complex structural parameters, the simplified 2D structures of hard carbons, prepared at different heating rates during the low temperature processing, are presented in Fig. 4. As can be seen, the slowest ramp results in an insignificantly larger interlayer distance, a_3, and average stacking size, L_c. In spite of the fact that the average pore size, l_{pore}, remains similar for both hard carbons, HC-2–600–1500 possesses more elongated pores (the highest value of l_c/l_p) and a narrower curvature of the graphene layer, l_R. The increase in the ramping rate leads to an enhancement in the internal structural order of HC-X–600–1500, as evidenced by the corresponding decreases in the values of parameter B_{fl} and parameter $\langle \Delta^2 a_3/{a_3}^2 + \Delta^2 l_R/{l_R}^2 \rangle$. This combination seems to be favorable for sodium storage. However, the structures in Fig. 4 are two-dimensional and simplified, and they do not consider variations in pore wall thicknesses, l_{solid}, and the volume of closed pores, $V_{closed\ pores}$, which are also significant (Table 1 and Table S6†). Additionally, they do not represent the types of defects, the degree of sodiation, and the detailed localization of sodium ions.

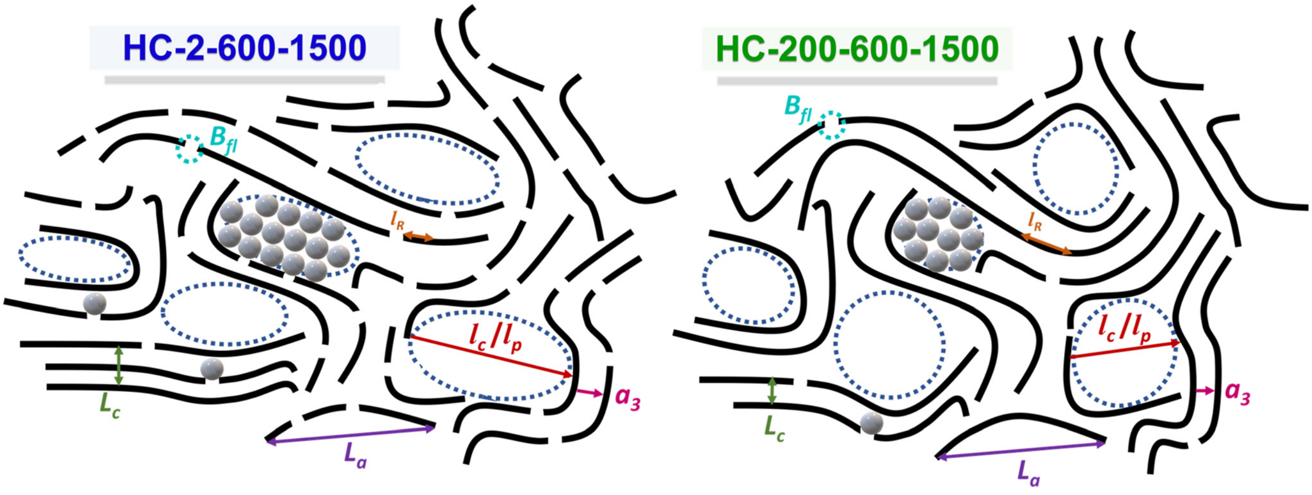

Fig. 4 Simplified 2D structures of hard carbons after pre-carbonization at different heating rates.

Conclusions

This study demonstrated the ability to control the structure of glucose-derived hard carbons by altering the heating rate of the initial temperature ramp rate during carbonization. Structural characterization of the investigated materials reveals that the heating rate during the critical low-temperature phase has minimal impact on the microstructure. Conversely, it significantly influences the mesostructure, which refers to the overall porosity. Hence, the material obtained at a slower heating rate during the pre-carbonization stage results in a larger contribution of open and closed porosity, variations in pore shape, and higher defectiveness after high-temperature treatment. These structural changes result in an enhancement in specific sodiation capacity in the second and fifth cycles, as well as the highest capacity of sodium electroplating below 0 V *vs.* Na/Na^+. This work proves that it is essential to maintain a slow heating rate during the pre-carbonization stage in order to obtain the most favorable hard carbon structure for storage applications. The appropriate control of HC's structure will lead to further enhancement of the negative electrode performance and the development of high-energy and cost-effective sodium-ion battery systems in the near future.

Conflicts of interest

There are no conflicts to declare.

Data availability

All relevant data are within the manuscript and the data supporting this article have been included as part of the ESI.† The raw dataset is openly available online in Radar4Chem through the following DOI: 10.22000/yumhgwcj7vv1q3py.

Acknowledgements

The research was supported by the Federal Ministry of Education and Research (BMBF) within the project NATTER under grant number 03XP0525E. Seed funding for this work has been provided by the project "CLUSTERBATT" within the Fraunhofer-MaxPlanck collaboration programme. We specifically acknowledge financial support by the European Fonds for Regional Development (Europäischer Fonds für Regionale Entwicklung; EFRE-OP 2021–2027; Project No. 2022 FGI 0007, DyNanoXRD). D. L. and M. H. would like to thank the German Chemical Industry Fund for financial support through a Liebig Fellowship. D. L. would like to thank the Carl-Zeiss Foundation for financial support within the Nexus programme.

References

1 S. C. Davis, S. E. Williams and R. G. Boundy, *Transportation Energy Data Book*, Oak Ridge, TN (United States), 35th edn, 2016.
2 A. Eftekhari, *ACS Sustainable Chem. Eng.*, 2019, **7**, 5602–5613.
3 T. Hettesheimer, C. Neef, I. Rosellón Inclán, S. Link, T. Schmaltz, F. Schuckert, A. Stephan, M. Stephan, A. Thielmann, L. Weymann and T. Wicke, *Lithium-Ion Battery Roadmap - Industrialization Perspectives toward 2030*, Fraunhofer ISI, 2023. DOI: 10.24406/publica-2153.
4 E. Petavratzi, D. Sanchez-Lopez, A. Hughes, J. Stacey, J. Ford and A. Butcher, *Miner. Econ.*, 2022, **35**, 673–699.
5 P. K. Nayak, L. Yang, W. Brehm and P. Adelhelm, *Angew. Chem., Int. Ed.*, 2018, **57**, 102–120.
6 R. Usiskin, Y. Lu, J. Popovic, M. Law, P. Balaya, Y.-S. Hu and J. Maier, *Nat. Rev. Mater.*, 2021, **6**, 1020–1035.
7 Y. Liu, B. V. Merinov and W. A. Goddard, *Proc. Natl. Acad. Sci. U. S. A.*, 2016, **113**, 3735–3739.

8 O. Lenchuk, P. Adelhelm and D. Mollenhauer, *Phys. Chem. Chem. Phys.*, 2019, **21**, 19378–19390.

9 A. Beda, F. Rabuel, M. Morcrette, S. Knopf, P. L. Taberna, P. Simon and C. M. Ghimbeu, *J. Mater. Chem. A*, 2021, **9**, 1743–1758.

10 S. Komaba, W. Murata, T. Ishikawa, N. Yabuuchi, T. Ozeki, T. Nakayama, A. Ogata, K. Gotoh and K. Fujiwara, *Adv. Funct. Mater.*, 2011, **21**, 3859–3867.

11 E. Irisarri, A. Ponrouch and M. R. Palacin, *J. Electrochem. Soc.*, 2015, **162**, A2476–A2482.

12 D. Saurel, B. Orayech, B. Xiao, D. Carriazo, X. Li and T. Rojo, *Adv. Energy Mater.*, 2018, **8**, 1703268.

13 X. Dou, I. Hasa, D. Saurel, C. Vaalma, L. Wu, D. Buchholz, D. Bresser, S. Komaba and S. Passerini, *Mater. Today*, 2019, **23**, 87–104.

14 X. Yuan, B. Zhu, J. Feng, C. Wang, X. Cai and R. Qin, *Chem. Eng. J.*, 2021, **405**, 126897.

15 Z. Jian, Z. Xing, C. Bommier, Z. Li and X. Ji, *Adv. Energy Mater.*, 2016, **6**, 1501874.

16 A. Kamiyama, K. Kubota, T. Nakano, S. Fujimura, S. Shiraishi, H. Tsukada and S. Komaba, *ACS Appl. Energy Mater.*, 2020, **3**, 135–140.

17 Z. Tian, Y. Zhang, J. Zhu, Q. Li, T. Liu and M. Antonietti, *Adv. Energy Mater.*, 2021, **11**, 2102489.

18 C. M. Ghimbeu, A. Beda, B. Réty, H. El Marouazi, A. Vizintin, B. Tratnik, L. Simonin, J. Michel, J. Abou-Rjeily and R. Dominko, *Adv. Energy Mater.*, 2024, **14**, 2303833.

19 J. S. McDonald-Wharry, M. Manley-Harris and K. L. Pickering, *Energy Fuels*, 2016, **30**, 7811–7826.

20 D. A. Stevens and J. R. Dahn, *J. Electrochem. Soc.*, 2000, **147**, 1271.

21 D. A. Stevens and J. R. Dahn, *J. Electrochem. Soc.*, 2001, **148**, A803.

22 D. A. Stevens and J. R. Dahn, *J. Electrochem. Soc.*, 2000, **147**, 4428.

23 J. M. Stratford, P. K. Allan, O. Pecher, P. A. Chater and C. P. Grey, *Chem. Commun.*, 2016, **52**, 12430–12433.

24 K. Gotoh, T. Yamakami, I. Nishimura, H. Kometani, H. Ando, K. Hashi, T. Shimizu and H. Ishida, *J. Mater. Chem. A*, 2020, **8**, 14472–14481.

25 Y. Morikawa, S. Nishimura, R. Hashimoto, M. Ohnuma and A. Yamada, *Adv. Energy Mater.*, 2020, **10**, 1903176.

26 E. Šić, K. Schutjajew, U. Haagen, H. Breitzke, M. Oschatz, G. Buntkowsky and T. Gutmann, *ChemSusChem*, 2024, **17**, e202301300.

27 Q. Meng, Y. Lu, F. Ding, Q. Zhang, L. Chen and Y.-S. Hu, *ACS Energy Lett.*, 2019, **4**, 2608–2612.

28 F. Xu, Y. Qiu, H. Han, G. Jiang, R. Zhao, E. Zhang, H. Li, H. Wang and S. Kaskel, *Carbon*, 2020, **159**, 140–148.

29 A. Kamiyama, K. Kubota, D. Igarashi, Y. Youn, Y. Tateyama, H. Ando, K. Gotoh and S. Komaba, *Angew. Chem., Int. Ed.*, 2021, **60**, 5114–5120.

30 K. Schutjajew, P. Giusto, E. Härk and M. Oschatz, *Carbon*, 2021, **185**, 697–708.

31 I. K. Ilic, K. Schutjajew, W. Zhang and M. Oschatz, *Carbon*, 2022, **186**, 55–63.

32 S. Prykhodska, K. Schutjajew, E. Troschke, L. Kaberov, J. Eichhorn, F. H. Schacher, F. Walenszus, D. Werner and M. Oschatz, *Energy Adv.*, 2024, **3**, 1342–1353.

33 J. R. Dahn, W. Xing and Y. Gao, *Carbon*, 1997, **35**, 825–830.

34 W. Xing, J. S. Xue and J. R. Dahn, *J. Electrochem. Soc.*, 1996, **143**, 3046–3052.

35 H. Au, H. Alptekin, A. C. S. Jensen, E. Olsson, C. A. O'Keefe, T. Smith, M. Crespo-Ribadeneyra, T. F. Headen, C. P. Grey, Q. Cai, A. J. Drew and M.-M. Titirici, *Energy Environ. Sci.*, 2020, **13**, 3469–3479.

36 M. P. Mercer, M. Nagarathinam, E. M. Gavilán-Arriazu, A. Binjrajka, S. Panda, H. Au, M. Crespo-Ribadeneyra, M. M. Titirici, E. P. M. Leiva and H. E. Hoster, *J. Mater. Chem. A*, 2023, **11**, 6543–6555.

37 E. Olsson, J. Cottom, H. Au, Z. Guo, A. C. S. Jensen, H. Alptekin, A. J. Drew, M. M. Titirici and Q. Cai, *Adv. Funct. Mater.*, 2020, **30**, 1908209.

38 M. M. Titirici, H. Alptekin, H. Au, A. C. S. Jensen, E. Olsson, M. Goktas, T. F. Headen, P. Adelhelm, Q. Cai and A. J. Drew, *ACS Appl. Energy Mater.*, 2020, **3**, 9918–9927.

39 C. M. Ghimbeu, J. Górka, V. Simone, L. Simonin, S. Martinet and C. Vix-Guterl, *Nano Energy*, 2018, **44**, 327–335.

40 Y. Li, Y. Lu, Q. Meng, A. C. S. Jensen, Q. Zhang, Q. Zhang, Y. Tong, Y. Qi, L. Gu, M. M. Titirici and Y. S. Hu, *Adv. Energy Mater.*, 2019, **9**, 1902852.

41 I. C. Lewis, *Carbon*, 1982, **20**, 519–529.

42 L. Yu, C. Falco, J. Weber, R. J. White, J. Y. Howe and M. M. Titirici, *Langmuir*, 2012, **28**, 12373–12383.

43 L. Xiao, H. Lu, Y. Fang, M. L. Sushko, Y. Cao, X. Ai, H. Yang and J. Liu, *Adv. Energy Mater.*, 2018, **8**, 1703238.

44 S. Guo, Y. Chen, L. Tong, Y. Cao, H. Jiao, Z. Long and X. Qiu, *Electrochim. Acta*, 2022, **410**, 140017.

45 Y. Zhen, Y. Chen, F. Li, Z. Guo, Z. Hong and M.-M. Titirici, *Proc. Natl. Acad. Sci. U. S. A.*, 2021, **118**, 100268.

46 X. Zhang, S. Han, C. Fan, L. Li and W. Zhang, *J. Solid State Electrochem.*, 2015, **19**, 715–721.

47 H. Yamamoto, S. Muratsubaki, K. Kubota, M. Fukunishi, H. Watanabe, J. Kim and S. Komaba, *J. Mater. Chem. A*, 2018, **6**, 16844–16848.

48 M. Oschatz, P. Pré, S. Dörfler, W. Nickel, P. Beaunier, J. N. Rouzaud, C. Fischer, E. Brunner and S. Kaskel, *Carbon*, 2016, **105**, 314–322.

49 W. Ruland and B. Smarsly, *J. Appl. Crystallogr.*, 2002, **35**, 624–633.

50 K. Faber, F. Badaczewski, W. Rul and B. M. Smarsly, *Z. Anorg. Allg. Chem.*, 2014, **640**, 3107–3117.

51 T. Pfaff, F. M. Badaczewski, M. O. Loeh, A. Franz, J.-U. Hoffmann, M. Reehuis, W. G. Zeier and B. M. Smarsly, *J. Phys. Chem. C*, 2019, **123**, 20532–20546.

52 O. Osswald and B. M. Smarsly, *C*, 2022, **8**, 78.

53 C. J. Jafta, A. Petzold, S. Risse, D. Clemens, D. Wallacher, G. Goerigk and M. Ballauff, *Carbon*, 2017, **123**, 440–447.

54 E. Härk, A. Petzold, G. Goerigk, M. Ballauff, B. Kent, U. Keiderling, R. Palm, I. Vaas and E. Lust, *Microporous Mesoporous Mater.*, 2019, **275**, 139–146.

55 E. Härk, A. Petzold, G. Goerigk, S. Risse, I. Tallo, R. Härmas, E. Lust and M. Ballauff, *Carbon*, 2019, **146**, 284–292.

56 K. Schutjajew, J. Pampel, W. Zhang, M. Antonietti and M. Oschatz, *Small*, 2021, **17**, 2006767.

57 J. T. Mckinnon, E. Meyer and J. B. Howard, *Combust. Flame*, 1996, **105**, 161–166.

58 R. Demir-Cakan, N. Baccile, M. Antonietti and M. M. Titirici, *Chem. Mater.*, 2009, **21**, 484–490.

59 H. N. Tran, F. C. Huang, C. K. Lee and H. P. Chao, *Green Process. Synth.*, 2017, **6**, 565–576.

60 S. M. Kwon, J. H. Jang, S. H. Lee, S. B. Park and N. H. Kim, *Wood Sci. Technol.*, 2013, **41**, 440–446.

61 R. J. White, C. Antonio, V. L. Budarin, E. Bergström, J. Thomas-Oates and J. H. Clark, *Adv. Funct. Mater.*, 2010, **20**, 1834–1841.

62 M.-M. Titirici, *Hydrothermal Carbonisation: A Sustainable Alternative to Versatile Carbon Materials Habilitationsschrift*, Max-Planck Institute für Kolloid und Grenzflächenforschüng, 2012.

63 A. C. Ferrari and J. Robertson, *Phys. Rev. B: Condens. Matter Mater. Phys.*, 2000, **61**, 14095–14107.

64 A. C. Ferrari and J. Robertson, *Phys. Rev. B: Condens. Matter Mater. Phys.*, 2001, **64**, 075414.

65 L. Kalder, A. Olgo, J. Lührs, T. Romann, R. Härmas, J. Aruväli, P. Partovi-Azar, A. Petzold, E. Lust and E. Härk, *Energy Storage Mater.*, 2024, **67**, 103272.

66 H. Fujimoto, *Carbon*, 2003, **41**, 1585–1592.

67 Y. Morikawa, S.-i. Nishimura, R.-i. Hashimoto, M. Ohnuma and A. Yamada, *Adv. Energy Mater.*, 2020, **10**, 1903176.

68 J. Song, B. Xiao, Y. Lin, K. Xu and X. Li, *Adv. Energy Mater.*, 2018, **8**, 1703082.

69 J. Meng, G. Jia, H. Yang and M. Wang, *Front. Chem.*, 2022, **10**, 986541.

70 M. Thommes, K. Kaneko, A. V. Neimark, J. P. Olivier, F. Rodriguez-Reinoso, J. Rouquerol and K. S. W. Sing, *Pure Appl. Chem.*, 2015, **87**, 1051–1069.

71 A. Beda, C. Vaulot and C. M. Ghimbeu, *J. Mater. Chem. A*, 2021, **9**, 937–943.

72 Y. Matsukawa, F. Linsenmann, M. A. Plass, G. Hasegawa, K. Hayashi and T.-P. Fellinger, *Beilstein J. Nanotechnol.*, 2020, **11**, 1217–1229.

73 L. Liu, S. (Johnathan) Tan, T. Horikawa, D. D. Do, D. Nicholson and J. Liu, *Adv. Colloid Interface Sci.*, 2017, **250**, 64–78.

74 A. Tóth and K. László, *Nov. Carbon Adsorbents*, Elsevier, 2012, pp. 147–171.

75 O. Osswald, M. O. Loeh, F. M. Badaczewski, T. Pfaff, H. E. Fischer, A. Franz, J. U. Hoffmann, M. Reehuis, P. J. Klar and B. M. Smarsly, *C*, 2023, **9**, 27.

76 M. Carboni, J. Manzi, A. R. Armstrong, J. Billaud, S. Brutti and R. Younesi, *ChemElectroChem*, 2019, **6**, 1745–1753.

77 E. Olsson, J. Cottom and Q. Cai, *Small*, 2021, **17**, 2007652.

78 Y. Youn, B. Gao, A. Kamiyama, K. Kubota, S. Komaba and Y. Tateyama, *npj Comput. Mater.*, 2021, **7**, 48.

79 B. Xiao, T. Rojo and X. Li, *ChemSusChem*, 2019, **12**, 133–144.